Graphene Plasmonic Tamm States with Ultracompact Footprint

Lei Wang,[1,2,*] Mengli Bie,[1] Wei Cai,[2,3,4,†] Xinzheng Zhang,[2,4,5] and Jingjun Xu[2,4,5,‡]
[1] *College of Physics and Electronic Engineering, Xinyang Normal University, Xinyang 464000, China*
[2] *The Key Laboratory of Weak-Light Nonlinear Photonics, Ministry of Education, School of Physics and TEDA Applied Physics Institute, Nankai University, Tianjin 300457, China*
[3] *Renewable Energy Conversion and Storage Center, Nankai University, Tianjin 300071, China*
[4] *Collaborative Innovation Center of Extreme Optics, Shanxi University, Taiyuan, Shanxi 030006, China*
[5] *Synergetic Innovation Center of Chemical Science and Engineering, Tianjin 300071, China*

(Received 16 May 2019; revised manuscript received 20 July 2019; published 27 August 2019)

In analogy to Tamm states in electronic systems, plasmonic Tamm states at the edge of terminated graphene plasmonic crystals are proposed. In contrast to plasmonic Tamm states that exist at the interface between metal-insulator-metal Bragg reflectors and metals, an edge-matching layer should be adopted to compensate the unique extra reflection phase at graphene terminals. The width of the edge-matching layer is optimized by the generalized Wiener-Hopf method according to the phase-matching condition. Moreover, graphene plasmonic crystals with merely two unit cells can compress electromagnetic fields into an extremely small mode volume with remarkable intensity enhancement by virtue of the graphene plasmonic Tamm states. Specifically, both the electric field and magnetic field intensities can be enhanced by 80 times in the ultracompact device with the length of 108.2 nm, which is more than 90 times shorter than the operation wavelength of 10 μm. The robust confinement mechanism of plasmonic Tamm states enables propagating plasmons trapping and enhancing the electromagnetic field in a planar landscape. Our results open an avenue for developing deep-subwavelength integrated graphene-based trappers, resonators, and biosensors and pave the way for ultracompact on-chip applications.

DOI: 10.1103/PhysRevApplied.12.024057

I. INTRODUCTION

Manipulation and concentration of the electromagnetic field at nanoscales is at the heart of nanophotonics and nanotechnology [1,2]. Graphene plasmons (GPs), the intrinsic collective excitations propagating along graphene sheets, have attracted much attention due to their highly controllable, extreme electromagnetic field confinement as well as long plasmonic lifetime [3–5]. Because of the unusually short wavelength relative to the free light, GPs can be used for enhancing light-matter interactions at deep-subwavelength scales. In recent years, plenty of graphene-based plasmonic devices with unique properties have been proposed theoretically and demonstrated experimentally, such as photodetectors [6], biosensors [7,8], resonators [9–11], perfect absorbers [12,13], and terahertz lasers [14,15]. Recently, Woessner *et al.* fabricated a graphene plasmonic phase modulator that can tune the phase between 0 and 2π *in situ* [16]. Amazingly, the length of the device is only 350 nm, which is more than 30 times shorter than the free-space wavelength. This result constitutes an important step for integrating plasmonic building blocks into a single graphene sheet. Moreover, energy storage devices such as resonators based on graphene ribbons [11] and disks [9,10,17] are also proposed to achieve the compact integrated optical circuits; however, these structures are fabricated by cutting the graphene into nanoscale structured patterns, which introduces large edge electron scattering losses and reduces the reusability of the graphene. In addition, the excitation process of cavity modes by ribbon [17] or tube [18] waveguides introduces extra undesired mode coupling losses, thus reducing the field enhancement. An available way to inhibit the losses is to combine the functionalities of power delivering and trapping simultaneously. In this spirit, tapered graphene waveguides [19] and spatially varying curvature resonators [20] are proposed to trap the propagating GPs. Nevertheless, their trapping ability is too weak to enhance the propagating GPs markedly.

On the other hand, plasmonic crystals, which can be regarded as photonic crystals composed of plasmonic materials [21–23], can also induce an energy band structure analogous to superlattices and photonic crystals. Moreover, the general Bloch-Floquet theorem in the periodically modulated equilibrium electron density of doped graphene induces energy gaps for GPs, which form the graphene plasmonic crystals (GPCs) [24]. Meanwhile, one

---

[*] nkwanglei@mail.nankai.edu.cn
[†] weicai@nankai.edu.cn
[‡] jjxu@nankai.edu.cn

can expect that the electromagnetic surface states such as Tamm states would exist at coated graphene terminals due to the strong Bragg scattering. As one of the surface Bloch states localized at interfaces of truncated crystalline materials, Tamm states have been extensively studied in superlattices [25], optical crystals [26], and plasmonic structures [27]. Unlike the conventional optical Tamm states [26] or plasmonic Tamm states [27], graphene plasmonic Tamm states (GPTSs) formed by GPs exist in deep-subwavelength graphene unit cells, which efficiently shrinks the device size and achieves large field enhancement.

In this paper, we show that GPTSs can be supported at the coated graphene terminals in graphene sheets with alternate chemical potentials, which is similar to traditional plasmonic Tamm states [27]. In contrast, an edge-matching layer should be introduced to satisfy the phase conditions originating from the unique reflection phase of GPs at the graphene terminals. Moreover, the generalized Wiener-Hopf method is adopted to optimize the width of the edge layer as well as calculate the reflectance spectra. As an example, the electric and magnetic field enhancement factors can be 9.5 and 9 in just 2 periods of the GPC, respectively. It is worth noting that the whole length of the coated graphene terminal is only 108.2 nm, which is just 1/92 of the operating wavelength 10 μm in vacuum. Such GPTSs can be used to trap and enhance the propagating edge modes in graphene sheets in an ultracompact way.

II. SIMULATION AND THEORY

It is well known that the dispersion relation of an encapsulated graphene monolayer is giving by

$$\frac{\epsilon_{1\parallel}}{\sqrt{\epsilon_{1\parallel}k_0^2 - q^2\epsilon_{1\parallel}/\epsilon_{1\perp}}} + \frac{\epsilon_{2\parallel}}{\sqrt{\epsilon_{2\parallel}k_0^2 - q^2\epsilon_{2\parallel}/\epsilon_{2\perp}}} = \frac{4\pi\sigma(\omega)}{\omega}, \tag{1}$$

where ϵ_1 and ϵ_2 are the permittivity of the superstrate and substrate, respectively. The extra subscripts denote the in-plane ($\parallel$) and out-of-plane ($\perp$) components provided that the materials are anisotropic. $q = q' + iq''$ is the propagation constant; thus, $\lambda_p = 2\pi/q'$ denotes the plasmon polariton wavelength and $k_0 = \omega/c$ is the wave number in vacuum. The complex cryogenic surface conductivity σ of the graphene monolayer is governed by the Kubo formula with the random phase approximations [28–30].

Our proposed viable high-mobility microdevice is based on a truncated graphene monolayer encapsulated in hexagonal boron nitride (hBN) with a structured heavily doped silicon back gate as shown in Fig. 1; different hBN thicknesses induce different Fermi energies under a back-gate bias voltage. GPs are launched (from $x < 0$) at normal incidence toward the graphene terminal coated by a GPC with two unit cells. The incident GPs in our configuration are coupled by gold antennas [31,32] from the photons in free space. Also, tip scattering coupling [33–36], sound-induced grating [37,38], and tapered bulk slabs [39] can excite the GPs as well. The mid-infrared light wavelength in vacuum is chosen to be around 10 μm ($\nu = 30$ THz) and the ambient temperature is set to 60 K. An honest value of cryogenic mobility $\mu = 10\ \mathrm{m}^2/\mathrm{Vs}$ is derived from the experiments [32]. The background Fermi energies are set to a fixed typical value $E_{F0} = 0.3$ eV derived from the experiments [32,40]. Actually, the permittivity of hBN in our considered range is simply assumed as the anisotropic single-Lorentzian model [32] $\epsilon_{\alpha\alpha}(\omega) = \epsilon_{\infty\alpha}[1 + \omega_{p\alpha}^2/(\omega_{t\alpha}^2 - \omega^2 - i\gamma_\alpha\omega)]$, $\alpha = x, z$, where the parameters are $\epsilon_{\infty x} = 4.90$, $\omega_{tx} = 1373/\mathrm{cm}$, $\omega_{px} = 869/\mathrm{cm}$, $\gamma_x = 5.5/\mathrm{cm}$, $\epsilon_{\infty z} = 2.95$, $\omega_{tz} = 760/\mathrm{cm}$, $\omega_{pz} = 346/\mathrm{cm}$, and $\gamma_z = 2.0/\mathrm{cm}$. Therefore, the frequency of the incident wave avoids both of the phonon modes simultaneously.

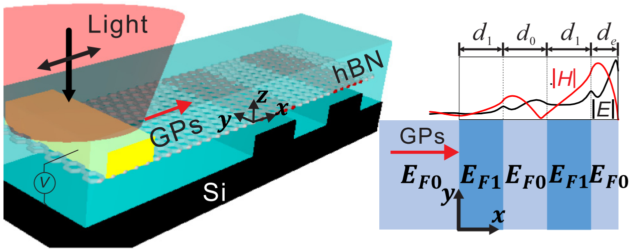

FIG. 1. A half-infinity graphene monolayer is encapsulated in a hBN environment, and a silicon layer with a two-raised-checker pattern is used to modulate its Fermi energy near the truncation. The layer widths of the conductivity pattern are $d_0 = d_1 = 30$ nm. The thickness of the hBN spacer is chosen large enough that the influence of the silicon on GPs can be ignored. A normally incident plasmon is impinging from the left side and trapped near the graphene terminal.

All of the numerical calculations are performed by a finite-element software package (COMSOL Multiphysics). In these calculations, graphene is modeled as a boundary condition characterized by its two-dimensional (2D) conductivity. When the modulated Fermi energies are set as $E_{F1} = 1.1$ eV, one can obtain the momentums $q_0' + iq_0'' = (129.92 + 0.547i)k_0$ and $q_1' + iq_1'' = (34.03 + 0.097i)k_0$ in the background and modulated zone, respectively. Taking both the Bragg condition $q_0'd_0 + q_1'd_1 = \pi$ and fabrication accuracy into consideration, we can obtain a Bragg reflector operating around $\lambda_B = 10\ \mu$m by choosing the period of the graphene waveguide as $d_0 = d_1 = 30$ nm; the dimensions are currently achievable with standard nanofabrication techniques such as focused ion beam etching and electron-beam lithography in conjunction with reactive ion etching. For the frequency interval corresponding to the center of a stopband, the width of the edge layer can be found from the well-known phase-matching condition

$$r_L r_R \exp(2i\delta_e) = 1, \tag{2}$$

where $r_L \equiv |r_{\rm GPC}| \exp(i\phi_{\rm GPC})$ is the reflection coefficient for the TM polarized wave of the Bragg reflector, $r_R \equiv |r_R| \exp(i\phi_R)$ is the reflection coefficient of the plasmon wave by an abrupt edge, and $\delta_e = q_0' d_e$ is the accumulated phase in the edge layer. The phase-matching condition requires that $\phi_R + \phi_{\rm GPC} + 2\delta_e = 2m\pi, m = 0, 1, 2, \ldots$. Using the analytical Wiener-Hopf method, the magnetic reflection coefficient r and transmission coefficient t for a normally incident plasmon wave at $i|j$ interfaces are found to be [41]

$$r_{ij} = \exp(i\theta_{ij}) \frac{q_i - q_j}{q_i + q_j}, \quad t_{ij} = t_{ji} = \frac{2\sqrt{q_i q_j}}{q_i + q_j}, \tag{3}$$

where the anomalous reflection phase θ_{ij} is given by

$$\theta_{ij} = -\theta_{ji} = \frac{\pi}{4} - \frac{2}{\pi} \int_0^\infty \frac{\arctan(q_i x / q_j)}{1 + x^2} dx. \tag{4}$$

Incidentally, one can find that the optical reciprocity relation $t_{ij} t_{ji} - r_{ij} r_{ji} = 1$ is still fulfilled. For an abrupt graphene edge, $q_R \to \infty (\mu_{cR} \to 0, \sigma_R \to 0)$, one has $r_R \approx \exp(-i3\pi/4)$ [42,43]; thus, the phase-matching condition gives $2\delta_e + \phi_{\rm GPC} = -\phi_R \approx 3\pi/4$ for $m = 0$. Moreover, the reflection coefficient of the GPs r_L is described by the superpositions of the secondary wave from each interface:

$$r_{01010} = r_{01} + \frac{t_{01} t_{10} r_{10} \exp(2i\delta_1)}{1 - r_{10} r_{10} \exp(2i\delta_1)} + \frac{t_{010} t_{010} r_{01} \exp(2i\delta_0)}{1 - r_{010} r_{01} \exp(2i\delta_0)} + \frac{t_{0101} t_{1010} r_{10} \exp(2i\delta_1)}{1 - r_{1010} r_{10} \exp(2i\delta_1)}, \tag{5}$$

where $\delta_0 = q_0' d_0$, $\delta_1 = q_1' d_1$ are the accumulated phases across each layer 0 and 1, and

$$r_{010} = r_{01} + \frac{t_{01} t_{10} r_{10} \exp(2i\delta_1)}{1 - r_{10} r_{10} \exp(2i\delta_1)}, \quad t_{010} = \frac{t_{01} \exp(i\delta_1) t_{10}}{1 - r_{10} r_{10} \exp(2i\delta_1)} \tag{6}$$

denote the reflectance and transmission of a Fabry-Perot (FP) cavity sandwiched by a 0|1 interface and a 1|0 interface [44]. Furthermore,

$$r_{0101} = r_{010} + \frac{t_{010} t_{010} r_{01} \exp(2i\delta_0)}{1 - r_{010} r_{01} \exp(2i\delta_0)}, \quad t_{0101} = \frac{t_{010} \exp(i\delta_0) t_{01}}{1 - r_{010} r_{01} \exp(2i\delta_0)}, \tag{7}$$

and

$$r_{1010} = r_{10} + \frac{t_{10} t_{01} r_{010} \exp(2i\delta_0)}{1 - r_{010} r_{01} \exp(2i\delta_0)}, \quad t_{1010} = \frac{t_{10} \exp(i\delta_0) t_{010}}{1 - r_{010} r_{01} \exp(2i\delta_0)} \tag{8}$$

can be regarded as the reflectance and transmission of the equivalent FP cavities sandwiched by an effective 01|0 interface and a 0|1 interface and by a 1|0 interface and an effective 0|10 interface, respectively.

Finally, the total reflection coefficient with the abrupt edge turns out to be

$$r = r_L + \frac{t_L^2 r_R \exp(2i\delta_e)}{1 - r_L r_R \exp(2i\delta_e)}, \tag{9}$$

where $t_L = t_{0101} \exp(i\delta_1) t_{10} / [1 - r_{10} r_{1010} \exp(2i\delta_1)]$ is the transmittance of the GPC, and the pole of r yields the phase-matching condition Eq. (2) as expected. Throughout this paper, the analytic reflectance spectra are computed using Eq. (9) and $R = |r|^2$.

III. RESULTS AND DISCUSSIONS

Noting that the forbidden band of the GPCs is a prerequisite to form the Tamm state, let us start by considering the band structure of GPCs. With the effective-index-based transfer matrix method, the band structure of a binary PC (plasmonic crystals) shown in Fig. 1 is found from the effective phase delay in a unit cell [23,24]:

$$\cos(k\Lambda) = \cos(q_1 d_1) \cos(q_0 d_0) - \frac{1}{2} \left(\frac{q_0}{q_1} + \frac{q_1}{q_0} \right) \sin(q_1 d_1) \sin(q_0 d_0), \tag{10}$$

where k is the Bloch vector of the GP modes and Λ is the period of the GPCs. The white regions illustrate the forbidden bands of the GPCs, and the star denotes the designed position to support the GPTSs. One can find that the bandwidths of the forbidden bands become wider as E_{F1} increases, which results from different variation amplitudes of the band minimum and maximum. Attributed to the large photonic density of states on the GP channel compared with the density of photonic radiating modes, the amplitude reflectance of an abrupt graphene truncation is virtually 100%. When the GPTSs are excited, electromagnetic fields are trapped and significantly Ohm damped. Hence, the condition of maximal field enhancement is the same as that of maximal power delivery in coated terminals, where the reflection minimum corresponds to the phase-matched wavelength. From the previous analysis, we know that the reflectance of the composite structure depends on the momenta of the GPs in each layer; thus, we visualize the dispersion and the quality factor $Q = q'/q''$

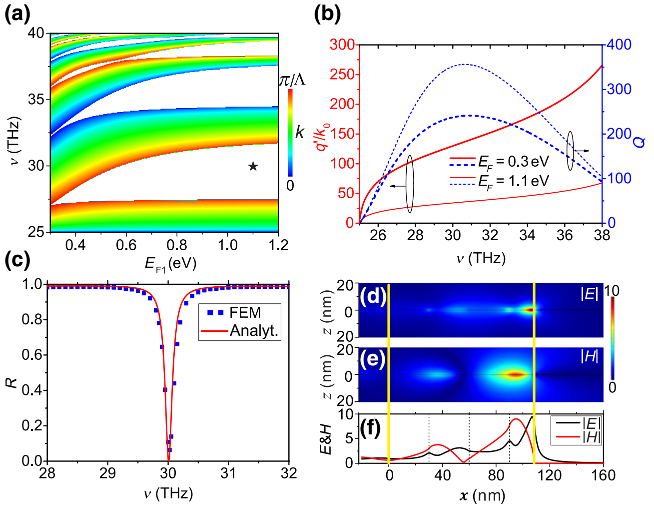

FIG. 2. The properties of the GPTSs. (a) Energy band diagram of the GPCs for different E_{F1} values. Here, the star denotes the parameters we adopt to construct the GPTSs. (b) Momentum ratios $\mathrm{Re}\{q_0/q_1\}$ and Q factor of the GPs for different modulation Fermi energies E_{F1}. (c) The reflection spectra of the configuration with the optimized width $d_e = 18.3$ nm for 2 periods; the minimum indicates the appearance of the GPTSs. (d),(e) The simulated electric field (d) and magnetic field (e) distributions at the operation wavelength 10 μm. (f) The cut lines of electromagnetic fields along $z = 1$ nm.

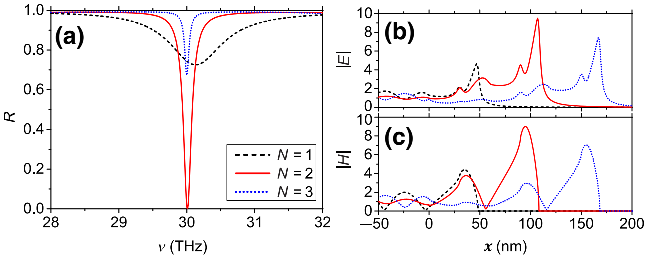

FIG. 3. (a) Reflection spectra of coated graphene terminals for different periods N. The reflection reaches a minimum of about 0.6% for $N = 2$. (b),(c) Normalized distributions of $|E|$ and $|H|$ of the electromagnetic field along the cut line $z = 1$ nm of the configuration for $N = 1$ (dashed line), 2 (solid line), and 3 (dotted line).

of the GPs in Fig. 2(b) at $E_{F0} = 0.3$ eV and $E_{F1} = 1.1$ eV, respectively. Both of these momenta increase along with the photon frequencies, while the quality factor reaches its maximum over 200 at a frequency of about 30 THz.

The reflectance calculated using Eq. (9) (solid red line) and the finite-element method (FEM) (marked by blue squares) is plotted in Fig. 2(c), where the optimized length of the edge layer is $d_e = 18.3$ nm for the generation of the GPTSs at $\lambda = 10$ μm and $E_{F1} = 1.1$ eV. There is a sharp dip with a minimum of 0.6% and FWHM of 0.14 THz. Incidentally, we find that the scattering of plasmons into photons at the interfaces is less than 2.1%, which verifies the excitation of GPTSs. In Figs. 2(d) and 2(e), the distributions of normalized $|H|$ and $|E|$ are plotted; the fields are extracted at 1 nm above the graphene. In the simulations, both electric and magnetic fields are normalized by the incoming values at $x = 0$. The dashed lines indicate the positions of discontinuous interfaces. It is obvious that both the electric and magnetic fields are confined and enhanced at the coated graphene terminal. The maximum $|E|$ occurs at the graphene truncation with an enhancement factor of 9.5, and the maximum $|H|$ occurs around the first interface near the GPC terminal with an enhancement factor of 9. It is worth noting that the phenomena are contrary to the behaviors in metal-insulator-metal-based plasmonic Tamm states [27], in which an edge layer should be introduced for the appearance of GPTSs. This effect can be ascribed to the extra reflective phase $\theta = \pi/4$ at the abrupt truncation. Moreover, the whole length of the device is only 108.2 nm, which means an ultracompact footprint with just 1/92 of the operating wavelength in vacuum. Furthermore, the ultrashort length does not sacrifice the field intensity enhancements of the terminal, which reaches as high as 90 as well.

Next, we focus on the influence of the period number N of GPCs on binding and exciting the GPTSs. The recurrence relations of the reflection coefficient for any layer are shown in the Appendix. The calculated reflection spectra for the coated graphene terminals with periods $N = 1$ (dashed line), 2 (solid line), and 3 (dotted line) are plotted in Fig. 3(a). The results illustrate that the full width at half maximum (FWHM) decreases while the reflectance reaches a minimum value for $N = 2$ as the number of periods increases.

The phenomena can be interpreted by the dual roles of the Bragg reflector, which works as an energy delivery as well as a reflector. Small numbers of periods are not able to confine enough energy at the graphene terminal, and long waveguides decrease the probability of the energy delivery and introduce more ohmic loss. For $N = 1$ or 3, the reflection minimum is about 70%; thus, most of the energy is reflected and only a small amount of energy is trapped at the terminal. As shown in Fig. 3(b), the maximum electric field enhancement drops from 9.5 for $N = 2$ to 7.4 for $N = 3$ or 4.6 for $N = 1$, and the magnetic field enhancement drops from 9 for $N = 2$ to 7 for $N = 3$ or 4.4 for $N = 1$ in Fig. 3(c), respectively.

In our proposed scheme, the edge-matching layer is indispensable to condense the extra reflection phase at the graphene edge. Because plasmon momenta are closely related with the Fermi energies of graphene, the terminal width d_e should be changed accordingly to the tuning of the Fermi energies at the designed operation wavelength. In Fig. 4(a), the dependence of reflectance on the modulated Fermi energies and terminal widths is demonstrated. The minimum of reflectance is consistent with the

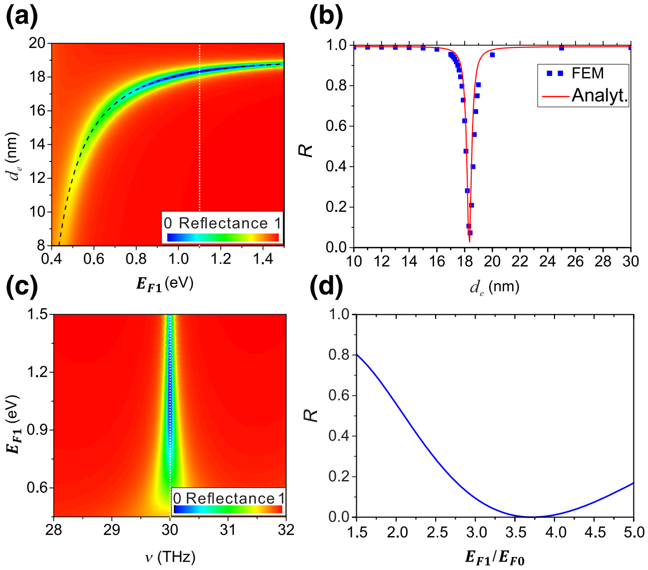

FIG. 4. (a) Reflectance of the coated graphene terminals for different terminal width d_e and modulated Fermi energies E_{F1}; here, E_{F0} is fixed at 0.3 eV. The dashed line represents the corresponding d_e derived from the phase-matching condition Eq. (2). (b) Reflectance of coated graphene terminals for different widths of edge-matching layer provided that $E_{F1} = 1.1$ eV. (c) Reflection spectra of the coated graphene terminals with d_e satisfying the phase-matching condition at designed photon frequencies. (d) Reflectance minimum of coated graphene terminals for different Fermi energies at designed photon frequencies.

results derived from the phase-matching condition. The reflectance of the configuration depending on the length of the edge layer at $E_{F1} = 1.1$ eV is enlarged in Fig. 4(b). The reflection local minimum indicates that the optimized length of the edge layer is $d_e = 18.3$ nm for generation of the GPTSs. The reflectances calculated using Eq. (9) (solid red line) and FEM (marked by blue squares) show excellent agreement. As designed, the reflection reaches a minimum of about 2.7% and the FWHM is only 0.4 nm, which makes it a potential sensitive detector in edge roughness detection. With the optimized terminal widths d_e, the reflection spectra for the coated graphene terminals with modulated Fermi energies E_{F1} from 0.45 to 1.5 eV are plotted in Fig. 4(c). With increasing Fermi energy contrast, the FWHM decreases. Figure 4(d) plots the reflectance minimum of the coated graphene terminals for different Fermi energies ratios E_{F1}/E_{F0} at the operation frequency $\nu = 30$ THz; the reflective minimum turns out to be less than 10% for $3E_{F0} \leq E_{F1} \leq 4.67E_{F0}$ in our configuration. In the contrast range of these Fermi energies, both the electric field and magnetic field enhancement are over 6.

As we know, Fermi energy as high as 1.1 eV is very hard to achieve without decreasing the mobility of graphene in real experiments. It is very necessary to explore the configuration with lower background Fermi energy as well as the modulated Fermi energy. Figures 5(a)–5(c) indicate that there are several local minimum regions for low E_{F0}, while these modes possess a very large slope with the Fermi energies and disappear for $E_{F0} \geq 0.2$ eV; as a result, these regions are too sensitive to the variation of Fermi levels. Moreover, one can find that the robust modes that lie at $E_{F1}/E_{F0} \geq 2.5$ always exist for any E_{F0}. In Fig. 5(d), we present the variation of the reflection with respect to the ratio or E_{F1}/E_{F0} with fixed ratios. One can find that the reflectance is near zero for $E_{F0} \approx 0.137$, 0.191, and 0.3 eV respectively when $E_{F1}/E_{F0} = 3.667$ and $E_{F0} \approx 0.128$ and 0.17 eV respectively when $E_{F1}/E_{F0} = 2.667$.

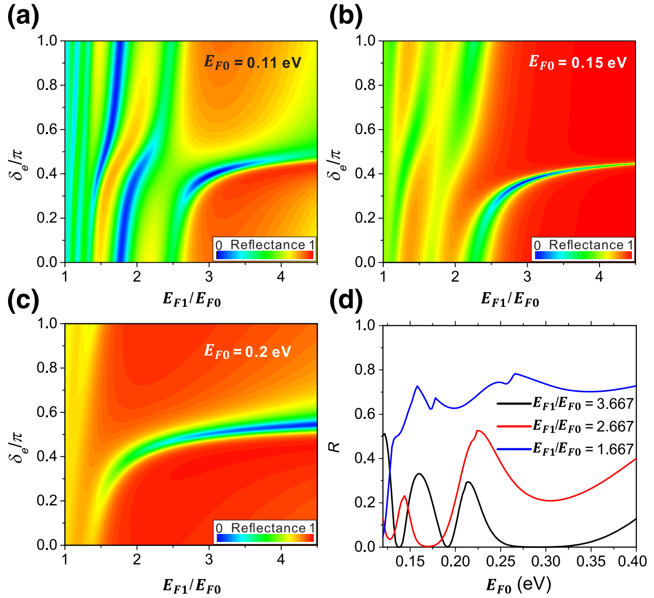

FIG. 5. (a)–(c) Reflectance of the coated graphene terminals for different accumulated edge phase δ_e and Fermi energy ratio E_{F1}/E_{F0} values; here, E_{F0} is fixed at (a) 0.11 eV, (b) 0.15 eV, and (c) 0.2 eV, respectively. (d) Reflectance minimum of coated graphene terminals for different background Fermi energies with fixed E_{F1}/E_{F0} at designed photon frequencies.

In our proposed scheme, the cryogenics play a vital role. Besides slightly modifying the Fermi energy of graphene, which can be compensated by a lower bias voltage in experiments, the intrinsic graphene and environmental dielectric losses are inhibited at low temperatures. Among them, the former contribution to the plasmonic scattering rate includes the acoustic phonon contribution $\gamma_A(T)$, intervalley electron-phonon scattering $\gamma_K(T)$, and electron-electron scattering [32]. These contributions can be attributed to the rise in graphene mobility. Experimental results show that the intrinsic plasmonic scattering rate dramatically drops from 20/cm to a value less than 2.0/cm [32], which is equivalent to the mobility of the graphene increasing from 1 m^2/Vs at room temperature to over 10 m^2/Vs at $T = 60$ K. To demonstrate the influence of this factor on the plasmonic edge states, we plot the dependence of the reflection spectra on the graphene mobility in

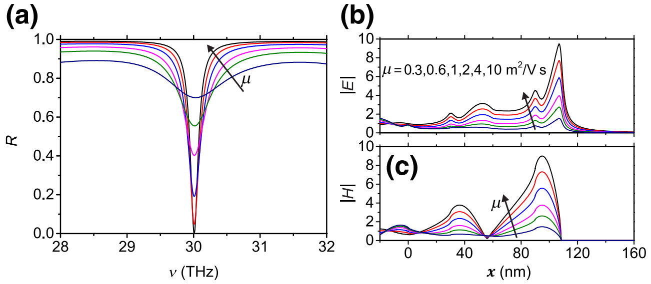

FIG. 6. (a) Reflection spectra of coated graphene terminals for different values of graphene mobility. (b),(c) Normalized distributions of $|E|$ and $|H|$ of electromagnetic fields along the cut line $z = 1$ nm of the configuration for different values of graphene mobility. The mobility μ increases from 0.3 to 10 $\mathrm{m^2/V\,s}$.

Fig. 6. As shown in Fig. 6(a), as the mobility μ drops from 10 $\mathrm{m^2/Vs}$ to 0.3 $\mathrm{m^2/Vs}$, the minimum values of reflectance increase monotonously from 0.6% to 70%, and the FWHW increases from 0.14 to 1.05 THz. Figures 6(b) and 6(c) plot the normalized distribution of $|H|$ and $|E|$ extracted at 1 nm above the graphene. One can find that the electric field enhancement drops from 9.5 to 1.54 and the magnetic field enhancement drops from 9 to 1.47. Next, we turn to see the effect of the cryogenics on environmental dielectric loss, i.e., the optical phonons of the hBN. Because of the low loss of hBN in our considered wavelength, the loss of the hBN does not apparently modify the reflectance spectra. More specifically, experimental results show that the damping constant γ of the hBN permittivity decreases from 3.4/cm at room temperature to 2.0/cm at $T = 60$ K, which leads to the maximum magnetic field enhancement slightly decreasing from 9 to 7.3 in our simulation.

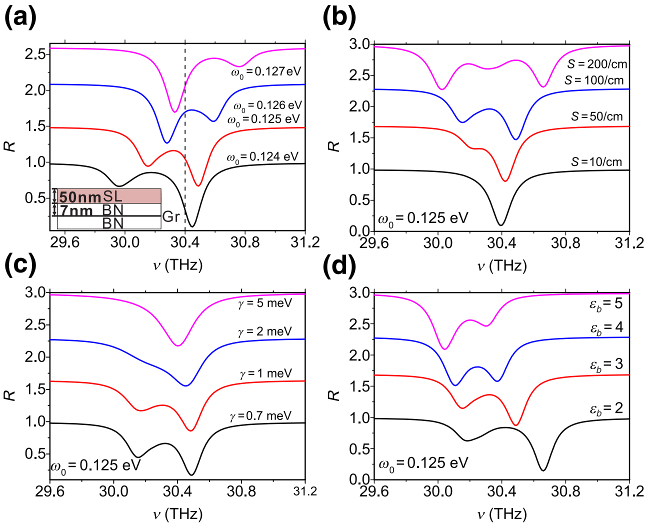

FIG. 7. (a) Reflection spectra of coated graphene terminals with a molecular layer for different transition energies of the molecular vibrations. The black vertical dashed line denotes the modified frequencies of GPTSs for $\epsilon_p = 3$. (b)–(d) Reflection spectra of coated graphene terminals with a molecular layer for different interaction parameter S (b), damping rate γ (c), and host dielectric ϵ_b (d), respectively.

Finally, we turn to explore the potential of GPTSs for enhancing IR absorption due to their excellent energy trapping and field enhancement. The mid-IR range encompassing the molecular vibrations is particularly well suited for biosensing. In order to take advantage of the enhanced near field, the thickness of superstrata is set as a typical value of 7 nm according to the experiment [40]. The sensor layer (SL) is deposited on the superstrata as shown in the inset of Fig. 7(a), the thickness of the sensor layer is set as 50 nm, and other parameters are the same as in Fig. 2. Here, the molecule layer is described in a simple way as a medium with a single Lorentzian resonance at the energy ω_0 by the following permittivity:

$$\epsilon_p(\omega) = \epsilon_b + \frac{S^2}{\omega_0^2 - \omega^2 - i\gamma\omega}, \tag{11}$$

where ϵ_b is the dielectric constant of the host matrix medium, $\hbar\omega_0$ are the absorption peaks, $\hbar\gamma$ is the total broadening of the molecular vibrations, and S is characterized by the concentration and oscillator strength. The parameter-dependent spectra for our proposed GPTSs is considered. In Fig. 7(a), the reflection spectra for the transition energy of molecules $\hbar\omega_0 = 0.124$, 0.125, 0.126, and 0.127 eV are shown. Here, $\epsilon_b = 3$, $\hbar\gamma = 0.7$ meV, and a typical value $S = 100$/cm are adopted [7,45]. One can find that the reflection valleys split into two valleys, and the valleys present anticrossing behavior, which denotes that the molecular vibrations are strongly coupled with the GPTSs. Both of the reflection valleys show blue-shift with the increase of transition energies of the molecules. Figure 7(b) shows how the spectra are affected by the interaction strength between molecules and GPTSs. Here, $\hbar\omega_0 = 0.125$ eV is adopted; the remaining parameters are the same as in Fig. 7(a). One can find that the spectra splitting is prominent for $S \geq 50$/cm, which makes it a very sensitive sensor in our considered range. Incidentally, we find that a third valley reappears at the frequencies of GPTSs for $S = 200$/cm, indicating the coexistence of a weak and strong coupling regime. On the other hand, the reflectance spectra with varied damping rates are represented in Fig. 7(c). One can find that the spectra splitting is prominent only for $\gamma \leq 2$ meV. In addition, the host dielectric dependence of reflection spectra is shown in Fig. 7(d). Since the frequencies of GPTSs undergo red-shift as the host dielectric ϵ_b increase, the two corresponding reflection valleys show red-shift accordingly.

IV. CONCLUSIONS

In this paper, a kind of GPTS at a coated graphene terminal is presented. In contrast to traditional plasmonic

Tamm states, an extra edge-matching layer is introduced to fulfill the phase-matching conditions between a GPC and an abrupt graphene terminal. Moreover, when the GPTSs are formed, the electromagnetic field enhances up to about 1 order of magnitude in the ultracompact device with length scaled down to 1/92 of the operating wavelength in vacuum. Our results can be further extended to other two-dimensional systems supporting plasmons (such as ultrathin metal films, topological insulators, black phosphorus, etc.), where the phase of the reflection coefficient suffers from similar anomalous mutations. Also, our analytical results and the associated physical insights into the plasmonic interaction with periodic modulated conductivity will facilitate the design of integrated narrow-band absorbers and trappers to enhance the propagating GPs on planar landscapes, providing significant applications in enhanced nonlinearities, biosensing, and surface-enhanced fluorescence in the mid-infrared range.

ACKNOWLEDGMENTS

L.W., W.C., X.Z., and J.X. acknowledge support from the National Natural Science Foundation of China (Grants No. 11604283, No. 91750204, No. 11774185, No. 61775106, and No. 11711530205); the Program for the National Key R&D Program of China (Grants No. 2017YFA0305100 and No. 2017YFA0303800); the Changjiang Scholars and Innovative Research Team in University (Grant No. IRT13_R29); the 111 Project (B07013); the Tianjin Natural Science Foundation (Grant No. 18JCQNJC02100); the Key Research Projects of Henan Provincial Department of Education (Grant No. 16A140048); and the Fundamental Research Funds for the Central Universities.

APPENDIX

The arbitrary layered configuration $1|2|3|\cdots|j|j+1$ can always be regarded as an effective FP cavity composed of a central layer j sandwiched by the effective interface $123\ldots j-1|j$ and the interface $j|j+1$, thus satisfying the recursion relation

$$\overrightarrow{r}_{i+1} = \overrightarrow{r}_i + \frac{\overrightarrow{t}_i\,\overleftarrow{t}_i\,r_{i(i+1)}\exp(2id_i)}{1-\overleftarrow{r}_i\,r_{i(i+1)}\exp(2id_i)}, \qquad \text{(A1)}$$

where $\overrightarrow{r}_i \equiv r_{123\cdots i}$ denote the positive sequence, implying the incident GPs impinging from the left side and propagating from layer 1 to layer i, while $\overleftarrow{r}_i \equiv r_{i(i-1)\cdots 321}$ denote the inverse sequence, implying the incident GPs impinging from the right side and propagating from layer i to layer 1. The transmission coefficients satisfy

$$\overrightarrow{t}_{i+1} = \frac{\overrightarrow{t}_i\,\exp(id_i)t_{i(i+1)}}{1-r_{i(i+1)}\,\overleftarrow{r}_i\,\exp(2id_i)}. \qquad \text{(A2)}$$

However, this is usually complicated because $\overrightarrow{r}_{i+1}$ depends on all four coefficients $\overrightarrow{r}_i$, $\overleftarrow{r}_i$, $\overrightarrow{t}_i$, and $\overleftarrow{t}_i$; thus, two auxiliary recursion relations about $\overleftarrow{r}$ and $\overleftarrow{t}$,

$$\overleftarrow{r}_{i+1} = r_{(i+1)i} + \frac{t_{(i+1)i}t_{i(i+1)}\,\overleftarrow{r}_i\exp(2id_i)}{1-\overleftarrow{r}_i r_{i(i+1)}\exp(2id_i)} \qquad \text{(A3)}$$

and

$$\overleftarrow{t}_{i+1} = \frac{\overleftarrow{t}_i\exp(id_i)t_{(i+1)i}}{1-\overleftarrow{r}_i r_{i(i+1)}\exp(2id_i)}, \qquad \text{(A4)}$$

have to be adopted to calculate these coefficients. Interestingly, in the binary PC structure, we have $\overleftarrow{r}_{01\cdots 10} = \overrightarrow{r}_{01\cdots 10} = r_{010\cdots 010}$ due to the mirror symmetry. Thus, there is no need to distinguish the direction of incidence for this kind of coefficient; that is, the vector symbols can be omitted as we do in Eq. (9). It allows for considerable computational savings.

[1] A. F. Koenderink, A. Alù, and A. Polman, Nanophotonics: Shrinking light-based technology, Science **348**, 516 (2015).

[2] W. L. Barnes, A. Dereux, and T. W. Ebbesen, Surface plasmon subwavelength optics, Nature **424**, 824 (2003).

[3] T. Low and P. Avouris, Graphene plasmonics for terahertz to mid-infrared applications, ACS Nano **8**, 1086 (2014).

[4] A. Grigorenko, M. Polini, and K. Novoselov, Graphene plasmonics, Nature Photon. **6**, 749 (2012).

[5] F. J. García de Abajo, Graphene plasmonics: Challenges and opportunities, ACS Photonics **1**, 135 (2014).

[6] Z. Sun and H. Chang, Graphene and graphene-like two-dimensional materials in photodetection: Mechanisms and methodology, ACS Nano **8**, 4133 (2014).

[7] D. Rodrigo, O. Limaj, D. Janner, D. Etezadi, F. J. García de Abajo, V. Pruneri, and H. Altug, Mid-infrared plasmonic biosensing with graphene, Science **349**, 165 (2015).

[8] L. Zundel and A. Manjavacas, Spatially resolved optical sensing using graphene nanodisk arrays, ACS Photonics **4**, 1831 (2017).

[9] A. Y. Nikitin, P. Alonso González, S. Vélez, S. Mastel, A. Centeno, A. Pesquera, A. Zurutuza, F. Casanova, L. E. Hueso, F. H. L. Koppens, and R. Hillenbrand, Real-space mapping of tailored sheet and edge plasmons in graphene nanoresonators, Nature Photon. **10**, 239 (2016).

[10] W. Luo, W. Cai, Y. Xiang, W. Wu, B. Shi, X. Jiang, N. Zhang, M. Ren, X. Zhang, and J. Xu, In-plane electrical connectivity and near-field concentration of isolated graphene resonators realized by ion beams, Adv. Mater. **29**, 1701083 (2017).

[11] V. W. Brar, M. S. Jang, M. Sherrott, J. J. Lopez, and H. A. Atwater, Highly confined tunable mid-infrared plasmonics in graphene nanoresonators, Nano Lett. **13**, 2541 (2013).

[12] S. Thongrattanasiri, F. H. L. Koppens, and F. J. García de Abajo, Complete Optical Absorption in Periodically Patterned Graphene, Phys. Rev. Lett. **108**, 047401 (2012).

[13] S. Kim, M. S. Jang, V. W. Brar, K. W. Mauser, L. Kim, and H. A. Atwater, Electronically tunable perfect absorption in graphene, Nano Lett. **18**, 971 (2018).

[14] M. Polini, Tuning terahertz lasers via graphene plasmons, Science **351**, 229 (2016).

[15] S. Chakraborty, O. P. Marshall, T. G. Folland, Y. J. Kim, A. N. Grigorenko, and K. S. Novoselov, Gain modulation by graphene plasmons in aperiodic lattice lasers, Science **351**, 246 (2016).

[16] A. Woessner, Y. Gao, I. Torre, M. B. Lundeberg, C. Tan, K. Watanabe, T. Taniguchi, R. Hillenbrand, J. Hone, M. Polini, and F. H. L. Koppens, Electrical 2π phase control of infrared light in a 350-nm footprint using graphene plasmons, Nature Photon. **11**, 421 (2017).

[17] L. Zhang, J. Yang, X. Fu, and M. Zhang, Graphene disk as an ultra compact ring resonator based on edge propagating plasmons, Appl. Phys. Lett. **103**, 163114 (2013).

[18] I. Soto Lamata, P. Alonso-González, R. Hillenbrand, and A. Y. Nikitin, Plasmons in cylindrical 2d materials as a platform for nanophotonic circuits, ACS Photonics **2**, 280 (2015).

[19] M. Miscuglio, D. Spirito, R. P. Zaccaria, and R. Krahne, Shape approaches for enhancing plasmon propagation in graphene, ACS Photonics **3**, 2170 (2016).

[20] D. Smirnova, S. H. Mousavi, Z. Wang, Y. S. Kivshar, and A. B. Khanikaev, Trapping and guiding surface plasmons in curved graphene landscapes, ACS Photonics **3**, 875 (2016).

[21] D. Chanda, K. Shigeta, T. Truong, E. Lui, A. Mihi, M. Schulmerich, P. V. Braun, R. Bhargava, and J. A. Rogers, Coupling of plasmonic and optical cavity modes in quasi-three-dimensional plasmonic crystals, Nat. Commun. **2**, 479 (2011).

[22] G. Vecchi, V. Giannini, and J. Gómez Rivas, Shaping the Fluorescent Emission by Lattice Resonances in Plasmonic Crystals of Nanoantennas, Phys. Rev. Lett. **102**, 146807 (2009).

[23] L. Wang, W. Cai, M. Bie, X. Zhang, and J. Xu, Zak phase and topological plasmonic Tamm states in one-dimensional plasmonic crystals, Opt. Express **26**, 28963 (2018).

[24] B. Shi, W. Cai, X. Zhang, Y. Xiang, Y. Zhan, J. Geng, M. Ren, and J. Xu, Tunable band-stop filters for graphene plasmons based on periodically modulated graphene, Sci. Rep. **6**, 26796 (2016).

[25] I. Tamm, On the possible bound states of electrons on a crystal surface, Phys. Z. Soviet Union **1**, 733 (1932).

[26] T. Goto, A. V. Dorofeenko, A. M. Merzlikin, A. V. Baryshev, A. P. Vinogradov, M. Inoue, A. A. Lisyansky, and A. B. Granovsky, Optical Tamm States in One-dimensional Magnetophotonic Structures, Phys. Rev. Lett. **101**, 113902 (2008).

[27] Y. Xiang, P. Wang, W. Cai, C.-F. Ying, X. Zhang, and J. Xu, Plasmonic Tamm states: Dual enhancement of light inside the plasmonic waveguide, J. Opt. Soc. Am. B **31**, 2769 (2014).

[28] B. Wunsch, T. Stauber, F. Sols, and F. Guinea, Dynamical polarization of graphene at finite doping, New J. Phys. **8**, 318 (2006).

[29] E. H. Hwang and S. Das Sarma, Dielectric function, screening, and plasmons in two-dimensional graphene, Phys. Rev. B **75**, 205418 (2007).

[30] V. P. Gusynin, S. G. Sharapov, and J. P. Carbotte, Unusual Microwave Response of Dirac Quasiparticles in Graphene, Phys. Rev. Lett. **96**, 256802 (2006).

[31] P. Alonso-González, A. Y. Nikitin, F. Golmar, A. Centeno, A. Pesquera, S. Vélez, J. Chen, G. Navickaite, F. Koppens, A. Zurutuza, F. Casanova, L. E. Hueso, and R. Hillenbrand, Controlling graphene plasmons with resonant metal antennas and spatial conductivity patterns, Science **344**, 1369 (2014).

[32] G. X. Ni, A. S. McLeod, Z. Sun, L. Wang, L. Xiong, K. W. Post, S. S. Sunku, B. Y. Jiang, J. Hone, C. R. Dean, M. M. Fogler, and D. N. Basov, Fundamental limits to graphene plasmonics, Nature **557**, 530 (2018).

[33] J. Chen, M. Badioli, P. Alonso-González, S. Thongrattanasiri, F. Huth, J. Osmond, M. Spasenović, A. Centeno, A. Pesquera, and P. Godignon, Optical nano-imaging of gate-tunable graphene plasmons, Nature **487**, 77 (2012).

[34] Z. Fei, A. Rodin, G. Andreev, W. Bao, A. McLeod, M. Wagner, L. Zhang, Z. Zhao, M. Thiemens, and G. Dominguez, Gate-tuning of graphene plasmons revealed by infrared nano-imaging, Nature **487**, 82 (2012).

[35] F. H. Koppens, D. E. Chang, and F. J. García de Abajo, Graphene plasmonics: A platform for strong light-matter interactions, Nano Lett. **11**, 3370 (2011).

[36] A. Y. Nikitin, F. Guinea, F. J. García-Vidal, and L. Martin-Moreno, Fields radiated by a nanoemitter in a graphene sheet, Phys. Rev. B **84**, 195446 (2011).

[37] J. Schiefele, J. Pedrós, F. Sols, F. Calle, and F. Guinea, Coupling Light into Graphene Plasmons through Surface Acoustic Waves, Phys. Rev. Lett. **111**, 237405 (2013).

[38] M. Farhat, S. Guenneau, and H. Bağcı, Exciting Graphene Surface Plasmon Polaritons through Light and Sound Interplay, Phys. Rev. Lett. **111**, 237404 (2013).

[39] A. Y. Nikitin, P. Alonso-González, and R. Hillenbrand, Efficient coupling of light to graphene plasmons by compressing surface polaritons with tapered bulk materials, Nano Lett. **14**, 2896 (2014).

[40] A. Woessner, M. B. Lundeberg, Y. Gao, A. Principi, P. Alonso-González, M. Carrega, K. Watanabe, T. Taniguchi, G. Vignale, M. Polini, J. Hone, R. Hillenbrand, and F. H. L. Koppens, Highly confined low-loss plasmons in graphene-boron nitride heterostructures, Nature Mater. **14**, 421 (2015).

[41] B. Rejaei and A. Khavasi, Scattering of surface plasmons on graphene by a discontinuity in surface conductivity, J. Opt. **17**, 075002 (2015).

[42] A. Y. Nikitin, T. Low, and L. Martin-Moreno, Anomalous reflection phase of graphene plasmons and its influence on resonators, Phys. Rev. B **90**, 041407(R) (2014).

[43] L. Du, D. Tang, and X. Yuan, Edge-reflection phase directed plasmonic resonances on graphene nano-structures, Opt. Express **22**, 22689 (2014).

[44] B.-Y. Jiang, E. J. Mele, and M. M. Fogler, Theory of plasmon reflection by a 1d junction, Opt. Express **26**, 17209 (2018).

[45] A. Marini, I. Silveiro, and F. J. García de Abajo, Molecular sensing with tunable graphene plasmons, ACS Photonics **2**, 876 (2015).